Modelling and experimental investigation of capsule-tumour contact for early bowel cancer detection

Jiyuan Tian[a], Yang Liu[a,*], Haohao Bi[b], Shyam Prasad[c], Caishan Liu[d]

[a]*Exeter Small-Scale Robotics Laboratory, Engineering Department, University of Exeter, North Park Road, Exeter, UK, EX4 4QF*
[b]*School of Science, Qingdao University of Technology, Qingdao, 266520, China*
[c]*Royal Devon University Healthcare NHS Foundation Trust, Barrack Road, Exeter, UK, EX2 5DW*
[d]*State Key Laboratory for Turbulence and Complex Systems, College of Engineering, Peking University, Beijing 100871, China*

Abstract

Tissue's mechanical properties, such as stiffness, are critical biomarkers that could be utilised to detect early stages of malignant transformation and distinguish between healthy and abnormal tissues. This paper studied a new method by using a capsule robot to evaluate the stiffness of bowel tumour for early bowel cancer detection and staging. Hertz contact theory was used to model capsule-tumour contact in an intestinal environment. Both lateral and vertical contacts were performed with finite element (FE) and experimental validations. Young's moduli of bowel tumours obtained by the proposed models were applied to FE models and then generated force-displacement curves to compare with experiments. Our comparative analysis shows that FE results are in good agreement with experimental results. The proposed method can be potentially used in real time for detecting early bowel cancer by using a capsule robot when self-propelling in the bowel.

Keywords: Young's modulus; Bowel cancer; Capsule robot; Hertz contact theory; Biomechanics

1. Introduction

Bowel cancer is the second most deadly cancer and the third most prevalent malignancy worldwide. In 2018, there were 1.8 million new cases of bowel cancer and 880,792 reported deaths, accounting for 10% of new cancer cases and deaths worldwide [1, 2], and the number of new cases may increase to 2.5 million in 2035 [3]. Bowel cancer is also a disease that is greatly affected by gender. According to the survey [4], the mortality rate of men is significantly higher than that of women. In the UK, it has become the third most common cancer in men and women, and the annual loss is about 1.6 billion pounds [5]. In the Europe, it is the second and third leading cause of cancer death in men and women, respectively, with an estimated over 242,000 deaths in 2018 [6] and 245,000 deaths in 2020 [7]. Although the incidence of bowel cancer occurs primarily in elderly people, population-based studies in many countries have found that the incidence of bowel cancer is increasing among adults younger than fifty [8]. Therefore, it is essential to detect the occurrence of cancer at an early stage and to evaluate the stage of cancer precisely, so as to be able to prolong the patient's life and ease the economic burden.

*Corresponding author. Tel: +44(0)1392-724654, e-mail: y.liu2@exeter.ac.uk.
Email addresses: jt535@exeter.ac.uk (Jiyuan Tian), bihaohao@mail.nwpu.edu.cn (Haohao Bi), shyamprasad@nhs.net (Shyam Prasad), liucs@pku.edu.cn (Caishan Liu)

The emergence of bowel cancer begins with the formation of polypoid protrusions due to endogenous (e.g., genomic instability [9]) and exogenous (e.g., environmental factors and lifestyle [10]) oncogenic factors, followed by the step that accelerates the development of histologically advanced cancers, and finally the step that converts the tumours to invasive carcinoma [11]. The duration of the polyp-to-cancer progression sequence is often estimated to average over 10 years, making it difficult to observe and track *in vivo* [12]. Once tumour cells are spread, they may pierce the colonic lining, invade surrounding tissue cells and metastasise to nearby organs, such as the liver [13], resulting in an advanced cancer that are tricky to be removed by treatments, such as surgery, radiation and chemotherapy. However, in recent decades, survival rate for bowel cancer has been much improved thanks to the primary and accessorial diagnostics, such as colonoscopy [14] and capsule endoscopy [15], which examine the colon as presented in Fig. 1(a) for detection of premalignant and malignant changes through visualisation of the colonic mucosa. For the recent works on early imaging-assisted cancer identification [16] and AI-assisted endoscopic diagnosis of cancer [17], the shape of the cancer was considered as the main feature to distinguish from the intestinal wall and haustral folds. Endoscopic observation of cancerous polyps in the intestinal lumen varies in shape, including well-defined smooth round, flat, lobulated, and irregularly shaped polyps [18]. However, most of the cancerous polyps are roughly enveloped by ellipsoidal surfaces [19] as illustrated in Fig. 1(b), and this approximation has been applied for polyp detection [20], bowel polyp dynamic feature selection [21] and colon polyp annotation [22].

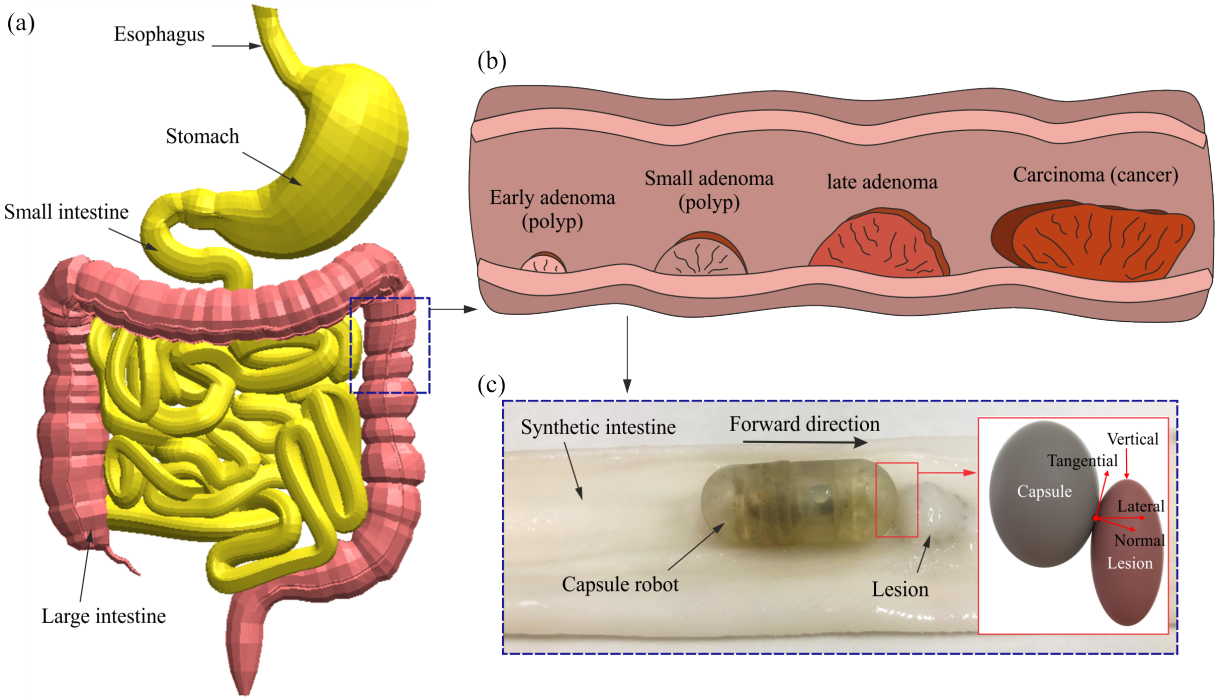

Figure 1: Schematic diagrams of (a) the digestive system and (b) the adenoma-carcinoma progression sequence. (c) Photograph of a capsule robot in contact with a tumour, and such a contact is considered as the contact between two ellipsoids shown in the blow-up window. Normal, tangential, vertical and lateral directions of contact are defined on the two ellipsoidal bodies.

For prognostic analysis of bowel cancer, tissue samples are usually taken during colonoscopy via biopsy [23] and further assayed and examined *ex vivo*. Such an examination will study the morphology, molec-

ular screening and pathogenesis of bowel cancer, including the identification of various biomarkers [24]. Numerous studies have found that as the stiffness of bowel cancer increases, the stage of cancer tends to be more advanced [25]. Therefore, the stiffness of bowel cancer has been regarded as the potential biomarker in recent years [26], with the ability to provide us the insights into the physiological and pathological processes at the cell, extracellular matrix, and tissue levels. Such a biomarker has become a macroscopic indicator for identifying the development stage and metastatic behaviour of cancer. Various techniques, such as atomic force microscopy [27], shear rheometer [28], tactile sensor [29], and ultrasound elastography [30], were developed to analyse the mechanical properties of soft biological samples. According to these tests, the mean values of Young's moduli of healthy bowel tissues range from 0.44 kPa to 9.9 kPa, whereas those of cancerous tissues including all bowel cancer stages measured by different techniques were summarised from 2.81 kPa to 157.3 kPa.

Since capsule endoscopy entered clinical practice, various driving modes [31–34] and functions have been developing in order to enable capsules to be accurately controlled in the gastrointestinal (GI) tract and achieve functions, such as drug delivery [35], biopsy [36] and cancer detection [37]. Particularly in cancer detection, current research works mainly focus on image-based analysis, such as matching endoscopic images with confirmed cancers through machine learning [38–40] and tumour-specific fluorescence imaging techniques [41]. To obtain the stiffness of bowel tumour, biopsy and further analysis in a biomedical laboratory are needed, which may cause secondary damage to the bowel and increase diagnosis costs that are burdensome for both patients and clinicians. In order to evaluate the stiffness of in-situ tumour for cancer detection and staging, the present work proposes to utilise the interactions between a capsule robot and the tumour. The robot could be any types of propulsion (e.g., [42],[43], [44] and [45]) but with a capsule profile as shown in Fig. 1(c). Once the displacement and contact force of the robot are measured by onboard sensors (e.g., displacement sensor and load cell), tumour's stiffness can be calculated in real time by using existing contact theories, such as Hertz contact theory.

The commonest shape of a capsule robot consists of a cylinder body with a hemispherical head and tail, and the shape of early cancer is a semi-ellipsoid. Capsule-tumour contact in the present work is thus considered as a sphere-ellipsoid contact as illustrated in the blow-up window of Fig. 1(c). As previous studies on capsule-tumour contact are very limited, modelling of sphere-ellipsoid contact can be referred to the contacts between two ellipsoidal particles of granular materials [46–49], soft finger contact mechanics [50–52] or mechanical properties of the skin based on the indentation method [53, 54]. Hertz contact, as the most basic and widely used theory of normal small deformation contact of linear elastic materials, was proposed in 1882 [55]. It does not consider the adhesion and friction forces between the contact surfaces but assumes that the contact area is much smaller than the size of the radius of the sphere. To extend Hertz theory to large deformations, Tatara [56] proposed a large deformation formulation for predicting the compression behaviour of elastic spheres. Furthermore, in 1971 Johnson, Kendall and Roberts proposed the so-called JKR contact mechanics model including surface adhesion [57], and Kuwabara and Kono extended the theory to viscoelastic particle contact theory in 1987 [58]. To account the effect of friction, Mindlin–Deresiewicz model was proposed with the consideration of tangential contact [59, 60] in 1949. As the bowel has rich intestinal mucus, the present work adopts a Hertz contact model assuming that the capsule-tumour contact is frictionless with a small deformation.

The purpose of this study is to evaluate the Young's moduli of in-situ tumours in different cancerous stages based on Hertz contact theory by using a capsule robot. According to the capsule-tumour contact shown in Fig. 1(c), the contact force between the capsule and tumour can be decomposed into normal and

tangential directions, and Young's modulus of the tumour can be evaluated from the normal displacement and force. The results of vertical compression tests usually used in *ex vivo* tests were compared with the results obtained from lateral compression. These two force-displacement results were obtained experimentally with capsule-tumour vertical and lateral compression contacts, and then were brought into the proposed models to obtain Young's moduli at small strains. To verify the effectiveness of the models, different force-displacement results were obtained by finite element (FE) modelling and compared with experimental results. The rest of this paper is organised as follows. In Section 2, mathematical modelling of the capsule robot encountering a tumour was presented. To obtain the surface parameters of capsule-tumour contact, characteristics of both contact surfaces were studied as special quadric surfaces. Coordinate of the contact point between the capsule and tumour was determined through analytic geometry, and then the capsule-tumour contact model based on Hertz contact theory was studied. To compare with capsule-tumour lateral contact, vertical compression modelling was further conducted considering a flat and a spherical indenters. Based on these models, corresponding FE simulations were performed and interpreted. In Section 3, vertical and lateral compression experiments were carried out. Thereafter, their comparison results and discussions were conducted in Section 4. Finally, concluding remarks and future works were drawn in Section 5.

2. Mathematical modelling of capsule-tumour contact

2.1. Preliminaries

For benign adenoma and post-cancerous tumour, their geometric surfaces are usually composed of quadratic surfaces with ellipsoids being one of the commonest shapes. Define $\vec{r} = (x, y, z)$ as a position vector on surface S relative to the origin of the orthogonal coordinate system. A point on surface can also be represented by a vector function, $\vec{r} = (x(u, v), y(u, v), z(u, v))$ or $\vec{r} = \vec{r}(u, v)$, where each coordinate is a function of two variables, u and v [61, 62]. It is known that curvature can be used to describe the shape of a surface. The first and second fundamental forms of the surface are associated with its curvature in terms of u and v as

$$\mathrm{I} = C\mathrm{d}u^2 + 2J\,\mathrm{d}u\,\mathrm{d}v + K\mathrm{d}v^2 \text{ and } \mathrm{II} = L\mathrm{d}u^2 + 2M\,\mathrm{d}u\,\mathrm{d}v + N\mathrm{d}v^2, \tag{1}$$

where C, J and K are the first fundamental coefficients, and L, M and N are the second fundamental coefficients [63]. Then the curvature k can be written as the ratio of the second fundamental form to the first one as

$$k = \frac{1}{R} = \frac{L\mathrm{d}u^2 + 2M\,\mathrm{d}u\,\mathrm{d}v + N\mathrm{d}v^2}{C\mathrm{d}u^2 + 2J\,\mathrm{d}u\,\mathrm{d}v + K\mathrm{d}v^2}, \tag{2}$$

where R is the radius of curvature of a curve passing through a point on the surface [62]. Define θ as the angle direction of the point, where $\tan\theta = \mathrm{d}v/\,\mathrm{d}u$, Eq. (2) can be rewritten as

$$k = \frac{1}{R} = \frac{L\cos^2\theta + 2M\sin\theta\cos\theta + N\sin^2\theta}{C\cos^2\theta + 2J\sin\theta\cos\theta + K\sin^2\theta}. \tag{3}$$

From Eq. (3), the maximum and minimum of curvature k yield two principal curvatures, and their corresponding angles θ are in two principal directions that are mutually orthogonal [62] given as

$$(CM - JL)\cos^2\theta + (CN - KL)\sin\theta\cos\theta + (JN - KM)\sin^2\theta = 0. \tag{4}$$

For a tri-axial ellipsoid with semi-axial lengths a, b, and c, its surface can be defined in the Cartesian coordinates as $x^2/a^2 + y^2/b^2 + z^2/c^2 = 1$. The coefficients of the first and second fundamental forms are obtained by the dot product of corresponding vectors [62, 64], which can be simplified as

$$C = \frac{a^4y^2}{b^4x^2} + 1, J = \frac{a^4yz}{b^2c^2x^2}, K = \frac{a^4z^2}{c^4x^2} + 1, L = \frac{a^4(c^2 - z^2)}{b^2c^2nx^3}, M = \frac{a^4yz}{b^2c^2nx^3}, \text{ and } N = \frac{a^4(b^2 - y^2)}{b^2c^2nx^3}, \quad (5)$$

where a vector normal to the surface is defined as $\vec{n} = \vec{r}_u \times \vec{r}_v$ and its length n is written as

$$n = \sqrt{1 + \frac{a^4y^2}{b^4x^2} + \frac{a^4z^2}{c^4x^2}}. \quad (6)$$

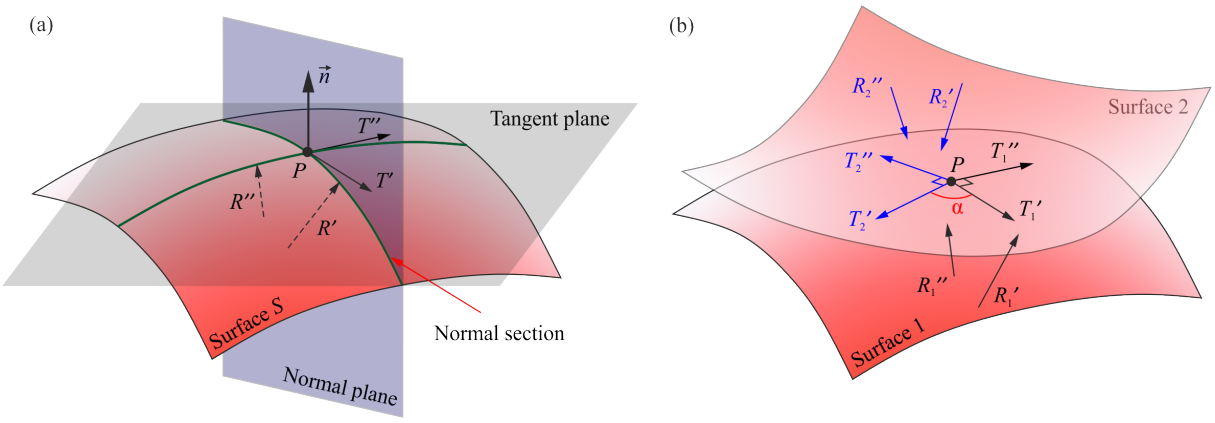

Figure 2: (a) Characteristics of a quadratic surface S at point P. Normal plane is generated by the normal vector $\vec{n}$ at point P on the surface. The intersection of the surface and the normal plane spans an infinite number of normal sections passing through point P, in which the maximum and minimum curvatures of the normal sections are the principal curvatures R_1' and R_1'', and their corresponding directions are the principal directions T_1' and T_1'', respectively. (b) Schematic of two contacting surfaces, Surfaces 1 and 2 with their principal radii of curvature, R_1' and R_1'' for Surface 1 and R_2' and R_2'' for Surface 2, and principal directions, T_1' and T_1'' for Surface 1 and T_2' and T_2'' for Surface 2 at contact point P. α is the inclined angle between two principal curvature directions from the two contact surfaces.

As illustrated in Fig. 2(a), the normal section at point P is the curve produced by the intersection of that surface with a normal plane. Through point P of the normal vector $\vec{n}$ and Surface S, and on the tangent plane, there are two principal (perpendicular) directions, T' and T'', for which the curvatures of their normal sections, R' and R'', namely the principal radii of curvatures based on Eq. (4), reach the maximum and minimum values, respectively. The principal radii of curvatures can be calculated using Eq. (3)-(6). Once the angle direction of the point, θ, is obtained from Eq. (4), its principal directions can be obtained as [64]

$$T = \cos\theta \begin{bmatrix} -\frac{a^2y}{b^2x} \\ 1 \\ 0 \end{bmatrix} + \sin\theta \begin{bmatrix} -\frac{a^2z}{c^2x} \\ 0 \\ 1 \end{bmatrix}. \quad (7)$$

When there are two surfaces contacting each other at point P, their principal radii of curvatures, R_1', R_1'', R_2' and R_2'', and corresponding principal directions, T_1', T_1'', T_2' and T_2'', are shown in Fig. 2(b), where α is the inclined angle between two principal curvature directions from the two contact surfaces

[64] given by

$$\cos\alpha = \frac{\langle {T_1}', {T_2}' \rangle}{\|{T_1}'\|_2 \|{T_2}'\|_2} = \frac{\langle {T_1}'', {T_2}'' \rangle}{\|{T_1}''\|_2 \|{T_2}''\|_2}. \tag{8}$$

2.2. Capsule-tumour lateral contact

The development of intestinal tumours commonly initiates within the epithelial lining of the intestinal mucosa. At the tissue level, when a polyp turns cancerous, with the gradual stiffening of the tumour bump within the intestinal lumen, the intestinal wall also stiffens synchronously as cancer cells gradually invade each intestinal layer (e.g. mucosa, submucosa, muscularis propria and serosa) and ultimately transforms into invasive cancer [11]. In addition, the large intestine wall has a very low degree of thickness, which is around 1.08 mm [65]. At the cellular level, a recent study [66] suggested that cell stiffness should be independent of its substrate mechanics, but at the millimetre-scale tissue level studied in this paper, for simplicity of the capsule-tumour contact model, the intestinal wall was considered as a single entity, with the stiffness of the tumour bump assumed to be equivalent to that of the underlying intestinal wall based on the reasons given above. Thus, the deformation of the tumour constitutes the primary focus of investigation during capsule-tumour contact, thereby neglecting the effect of the intestinal wall in this study.

During a practical procedure of capsule endoscopy, the capsule robot moves along the colon as presented in Fig. 1(c). When the capsule encounters a tumour, its head will be in contact first, leading to a sphere-ellipsoid contact shown in Fig. 3(a). The spherical head of the capsule is a special ellipsoid, for which the radius of principal curvature ${R_1}'$ and ${R_1}''$ at any point on the surface are equal to the radius of the sphere R_1, and the corresponding principal directions ${T_1}'$ and ${T_1}''$ are the same in any directions. The head of the spherical capsule with central point O_1 moving in the negative direction of X-axis under force F contacts ellipsoidal tumour with central point O_2 at point P_1. The radii of principal curvatures of ellipsoidal tumour at the contact point are ${R_2}'$ and ${R_2}''$, and the corresponding principal directions are ${T_2}'$ and ${T_2}''$. If the angle of initial contact is θ_1, when the capsule moves to ${O_1}'$, and the contact point moves to ${P_1}'$, the angle θ_1 becomes ${\theta_1}'$. If the largest cross-section of a sphere and the largest cross-section of an ellipsoid coincide in the same plane, this three-dimensional contact model can be simplified to two-dimensional as presented in Fig. 3(b). According to the plane coordinates (X, Y) with the ellipse centre O_2 as the origin point, the coordinate of centre of the capsule head O_1 with radius R_1 is (m, R_1), the coordinate of P_1 is (x_1, y_1), and the coordinate of P_2 is $(n, 0)$, where P_2 is the focal point of line O_1P_1 and X-axis.

Based on the geometric relationship between the capsule and the tumour shown in Fig. 3(a), the following assumptions are considered.

- Spherical capsule head moves in X direction only, and there is no rotation for the sphere.
- Tumour's strain is very small, so $\theta_1 = {\theta_1}'$.
- Contact area is very small comparing to the areas of capsule's head and tumour.
- Contact is frictionless.
- Tangential force F_t and displacement t_t are negligible.

By using the above assumptions, geometric similarity (see the red and green triangles in Fig. 3(b)) can be used to convert the horizontal force F and displacement t to the normal force F_n and displacement t_n perpendicular to the tangential line. Then Young's modulus of the tumour can be obtained by using Hertz contact theory [67].

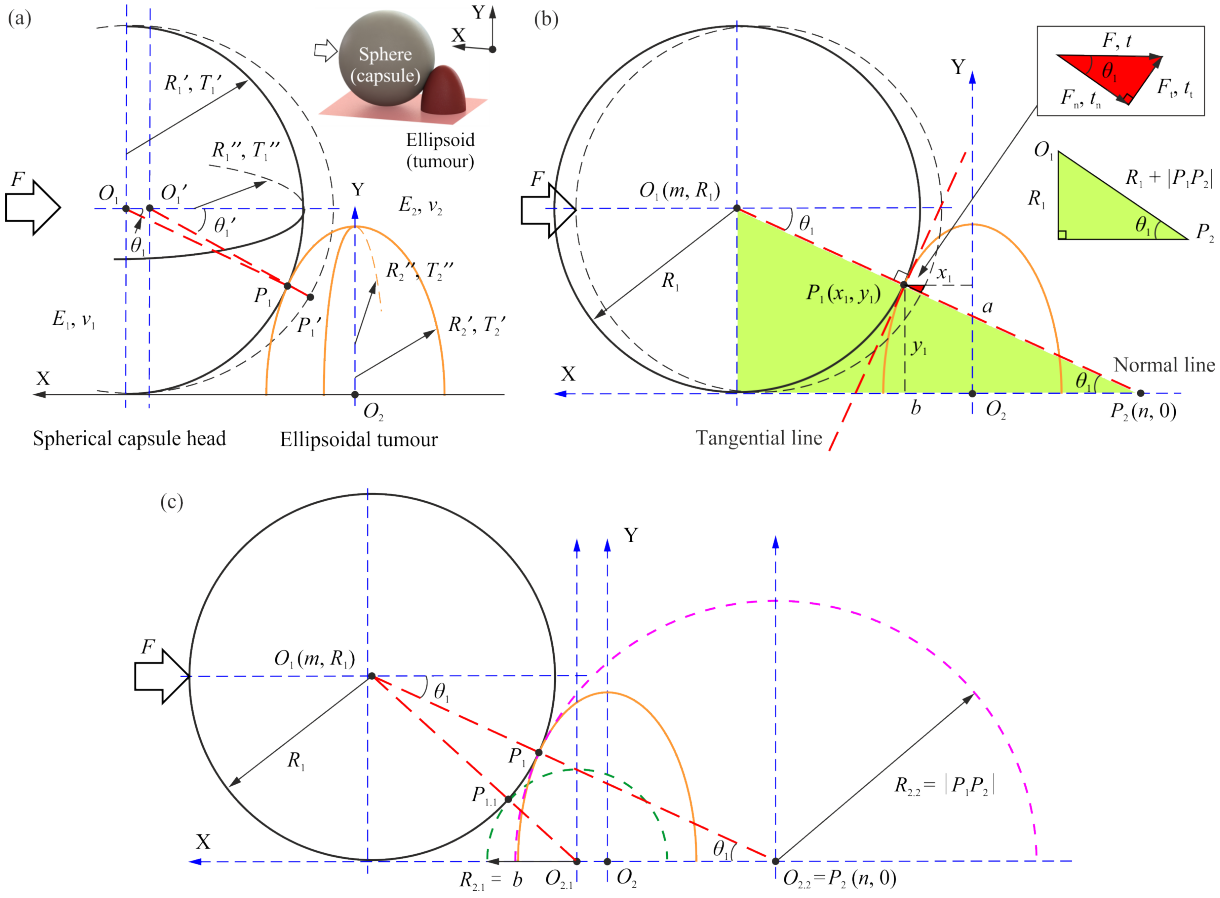

Figure 3: (a) General schematic of sphere-ellipsoid lateral contact for capsule-tumour interaction. (b) Two-dimensional schematic of sphere-ellipsoid lateral contact. (c) Sphere-ellipsoid lateral contact is extended to sphere-sphere contact.

When the capsule and the tumour are in contact, a small force F and a corresponding small displacement t are generated along X-axis direction, and these two solids deform and form an elliptical contact area. The equivalent Young's modulus of this contact can be expressed as [49, 54, 67]

$$E^* = \frac{3}{4} R_e^{-\frac{1}{2}} F_c^{\frac{3}{2}} F_n t_n^{-\frac{3}{2}} = \left(\frac{1-\nu_1^2}{E_1} + \frac{1-\nu_2^2}{E_2} \right)^{-1}, \tag{9}$$

where E_1 and E_2 are Young's moduli of the capsule and tumour, and ν_1 and ν_2 are their Poisson's ratios, respectively. F_n and t_n are the normal force and displacement, respectively, along the line P_1P_2 caused by F and t in X-axis. $R_e = \frac{1}{2}(AB)^{-1/2}$ is the equivalent contact radius, where A and B are obtained

from local geometry variables as

$$
\begin{aligned}
A+B &= \frac{1}{2}\left(\frac{1}{{R_1}'}+\frac{1}{{R_1}''}+\frac{1}{{R_2}'}+\frac{1}{{R_2}''}\right),\\
B-A &= \frac{1}{2}\left[\left(\frac{1}{{R_1}'}-\frac{1}{{R_1}''}\right)^2+\left(\frac{1}{{R_2}'}-\frac{1}{{R_2}''}\right)^2+2\left(\frac{1}{{R_1}'}-\frac{1}{{R_1}''}\right)\left(\frac{1}{{R_2}'}-\frac{1}{{R_2}''}\right)\cos 2\alpha\right]^{\frac{1}{2}},
\end{aligned}
\tag{10}
$$

where α is the angle of inclination between the two principal curvature directions derived from Eq. (8) for the two contact surfaces. F_c is the correction factor for the non-circularity of the contact area given as [68]

$$
F_c = 1-\left[\left(\frac{B}{A}\right)^{0.0684}-1\right]^{1.531}. \tag{11}
$$

In the present study, since the capsule shell is made of polythene, which is much stiffer than the tumour, it gives $E_1 \gg E_2$, so Eq. (9) becomes

$$
E^* \approx \left(\frac{1-{\nu_2}^2}{E_2}\right)^{-1}. \tag{12}
$$

In addition, Poisson's ratio of the tumour ν_2 is about 0.5 as the tissue is mostly composed of water which can be regarded as an incompressible material. Therefore, Young's modulus of the ellipsoidal tumour can be written as

$$
E_2 = \frac{9}{16}{R_e}^{-\frac{1}{2}}{F_c}^{\frac{3}{2}}F_n{t_n}^{-\frac{3}{2}}. \tag{13}
$$

According to Fig. 3(b), the coordinate of the contact point P_1, (x_1, y_1), is related to the coordinates of O_1 and O_2. If the coordinate of O_1 is (m, R_1), capsule's spherical profile can be written as $(x-m)^2+(y-R_1)^2={R_1}^2$, and the tumour's elliptic profile is written as $x^2/b+y^2/a=1$ if the coordinate of O_2 is $(0,0)$. The coordinate of P_1 can be determined by using trigonometric functions leading to $(x_1, y_1) = (m-R_1\cos\theta_1, R_1-R_1\sin\theta_1)$. The slope of tangential line of the contact point can be determined from the circle O_1 and the ellipse O_2 as $k_{t1}=1/\tan\theta_1$ and $k_{t2}=a^2x_1/b^2y_1$, respectively. If $P_2(n,0)$ is the intersection of O_1P_1 with X-axis, the coordinate of P_1 can be obtained from

$$
\begin{cases}
\dfrac{(m-R_1\cos\theta_1)^2}{b^2}+\dfrac{(R_1-R_1\sin\theta_1)^2}{a^2}=1,\\
\tan\theta_1=\dfrac{R_1}{m-n}=\dfrac{b^2(R_1-R_1\sin\theta_1)}{a^2(m-R_1\cos\theta_1)},
\end{cases}
\tag{14}
$$

where $m>0$ and $n<0$.

In order to validate whether ellipsoidal tumour can be assumed as a spherical shape for calculating its Young's modulus, two-dimensional models of sphere-sphere lateral contact are presented in Fig. 3(c), where both semicircle $O_{2.1}$ (dashed green line) with radius $R_{2.1}=b$ (the length of the semi-axial of the ellipse O_2) and semicircle $O_{2.2}$ (dashed magenta line) with radius $R_{2.2}=|P_1P_2|$ are externally tangent with the capsule (circle O_1). The comparison results will be presented and discussed in Section 4.

2.3. Normal compression

In general, Young's modulus of bowel tissue can be determined through *ex vivo* normal compression test on a tissue sample obtained via biopsy. Either by using atomic force microscopy [27] or tactile sensors [29], the onboard spherical indenter will be used to compress a flat-open tissue sample, and tissue

stiffness can be measured based on Hertz contact theory. In the present study, to compare with the sphere-ellipsoidal lateral contact shown in Fig. 3, normal compression modellings of the semi-ellipsoidal tumour compressed by a flat and a spherical indenters were carried out as presented in Fig. 4.

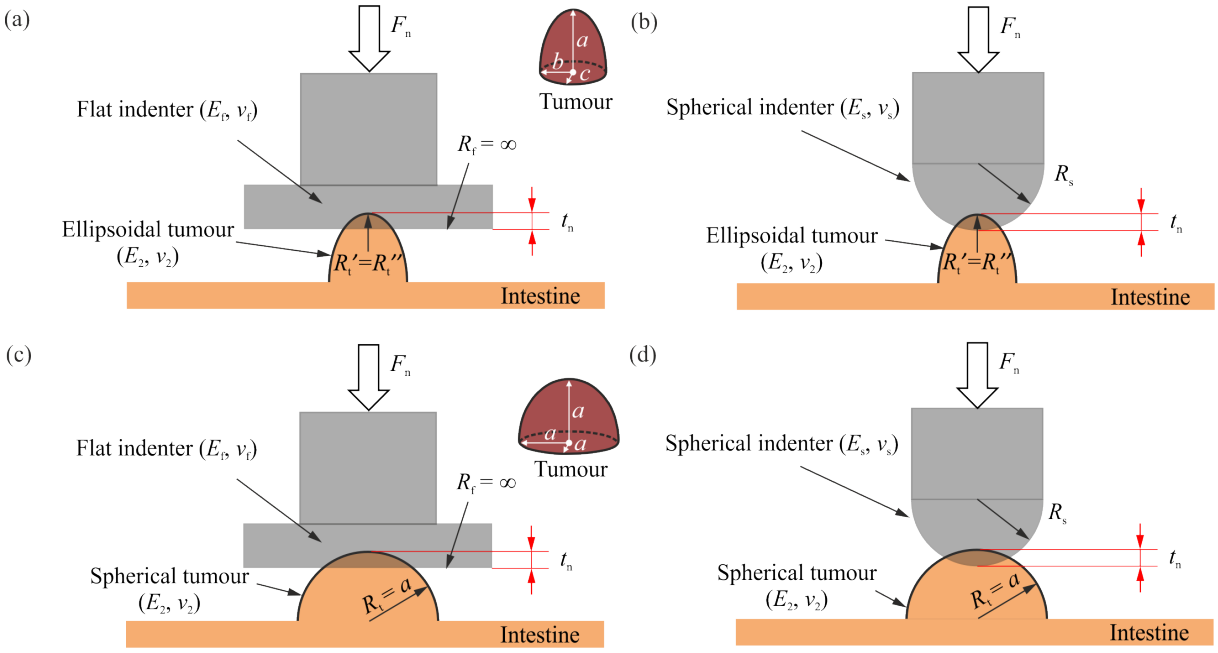

Figure 4: Two-dimensional schematic diagram of the tumour compressed by a flat and a spherical indenters, where the plane-ellipsoid and the sphere-ellipsoid vertical contacts are shown in (a) and (b), respectively. Spherical tumours were also considered, where the radius of the sphere R_t is equal to the height of the ellipsoidal tumour a, and such plane-sphere and sphere-sphere vertical contacts are shown in (c) and (d), respectively.

As seen from Fig. 4(a), the initial position of plane-ellipsoid contact is on the top point of the ellipsoid. Since it is compressed by a flat indenter, the radius of the flat indenter R_f can be regarded as infinite, and it has no radius of curvature. When the tumour is a special ellipsoid, where its semi-axis lengths are a, b and c ($b = c$), according to Eqs. (3)-(6), the principal radii of curvature at the top point of the ellipsoid are equal, i.e., ${R_t}' = {R_t}''$. Then Eq. (10) can be rewritten as $A = B = \frac{1}{2}{R_t}'$ as the principal directions can be any direction in the contact area, $F_c = 1$ and $R_e = {R_t}'$. When $E_f \gg E_2$ and $\nu_2 \approx 0.5$, Eq. (13) can be expressed as

$$E_2 = \frac{9}{16}{R_t}'^{-\frac{1}{2}} F_n {t_n}^{-\frac{3}{2}}. \tag{15}$$

Thus, once ${R_t}'$, F_n and t_n are known, Young's modulus of the tumour E_2 can be calculated.

In Fig. 4(b), the tumour is compressed by a spherical indenter. Its principal radii of curvature at any point of the sphere are equal to the radius of the sphere R_s, i.e., ${R_s}' = {R_s}'' = R_s$. The dimension of the tumour is the same as the case with the flat indenter, so ${R_t}' = {R_t}''$ at the top point of ellipsoidal tumour. Eq. (10) thus can be obtained as $A = B = \frac{1}{2}(\frac{1}{R_s} + \frac{1}{{R_t}'})$, and $F_c = 1$. Here, the equivalent contact radius R_e for sphere-ellipsoid contact is equal to $(\frac{1}{R_s} + \frac{1}{{R_t}'})^{-1}$. When $E_s \gg E_2$ and $\nu_2 \approx 0.5$, Eq. (13) can be written as

$$E_2 = \frac{9}{16}\left(\frac{1}{R_s} + \frac{1}{{R_t}'}\right)^{\frac{1}{2}} F_n {t_n}^{-\frac{3}{2}}. \tag{16}$$

Once R_s, ${R_t}'$, F_n and t_n are known, Young's modulus of the ellipsoid E_2 can be obtained. Furthermore, to

compare the ellipsoidal and spherical tumours, the contacts with a spherical tumour by using a flat and a spherical indenters were also modelled as illustrated in Figs. 4(c) and (d), respectively. The corresponding results will be studied in Section 4.

2.4. FE modelling

In order to verify the mathematical models studied above, FE modelling of the capsule-tumour lateral and vertical contacts were carried out by using ANSYS WORKBENCH 19.0/Static structural module as shown in Fig. 5. FE results were obtained based on elastic material constitutive, geometric relations, contact relations, boundary constraints and loads without involving any assumptions, thus providing a good reference for verifying the theoretical results.

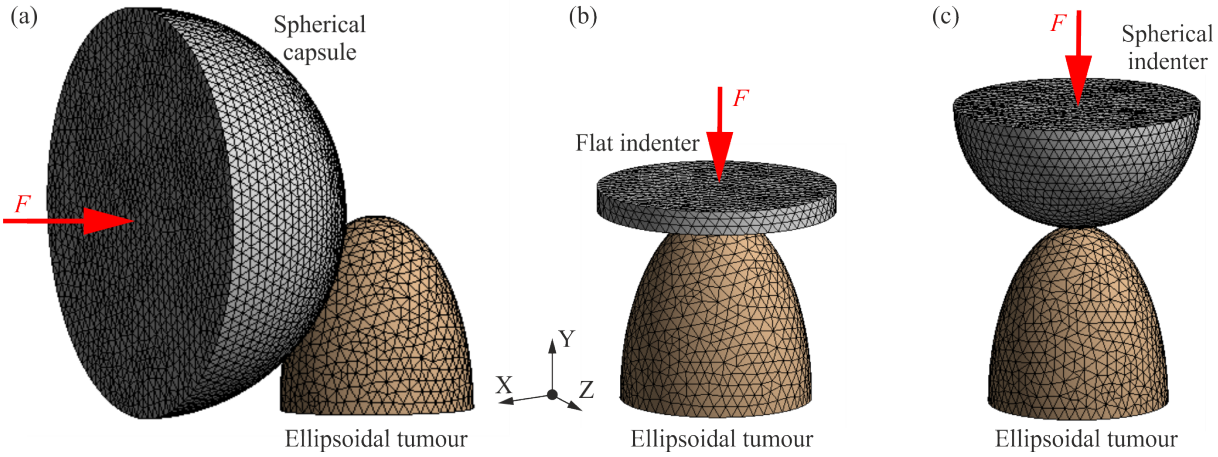

Figure 5: FE models of (a) the capsule-tumour lateral contact, (b) the vertical compression using a flat indenter and (c) the vertical compression using a spherical indenter.

As shown in Fig. 5(a), the spherical capsule has lateral contact with the fixed ellipsoidal tumour. In the FE model, all the rotational degrees of freedom of the sphere were restricted, and its displacement was only allowed along X-axis. In Figs. 5(b) and (c), both the flat and spherical indenters were vertically compressed on the fixed ellipsoidal tumour along Y-axis. Likewise, these two indenters only can move along Y-axis, and all their rotations were restricted. Furthermore, all dimensions in FE models were set the same as the dimensions of the experimental studies in Section 3. FE meshes were refined, and mesh convergence test was carried out to ensure computational accuracy. It is worth noting that during the actual process of our vibro-impact capsule, the driving force of the capsule ranges from 0.06 N to 0.2 N [69], which is consistent with the force exerted on the tumour at 10% compressive strain. Thus, in this study, we will focus on tumour deformation under 10% compressive strain in all models, providing more valuable references. For the capsule-tumour lateral contact model, the compression strain is defined as the ratio of tumour deformation along the normal direction (P_1P_2) of the capsule-tumour contact point to $|P_1P_2|$ shown in Fig. 3 (b). In vertical compression, its strain is the ratio of the amount of deformation in the vertical direction of the tumour to the total height of the tumour.

3. Experiment set-ups

This section studies the experiments for capsule-tumour lateral and vertical contacts. For lateral contact, an experimental testing rig was developed to record the force and displacement of the capsule

when contacting with the tumour. Schematic diagram of the testing rig is shown in Fig. 6, and its photograph is presented in Fig. 7(a) with two detailed views in (b) and (c). The capsule (indenter) that was made of polythene with a diameter of 17 mm sits on the intestine with a fixed block on top allowing its movement along lateral direction only. To reduce the influence of friction, lubricating gel was applied around the indenter. The ellipsoidal tumour with $a = 8$ mm and $b = c = 4$ mm consisted of an inner soft ellipsoid-shaped block covered by the thin layer of a synthetic intestine [70]. In order to vary the stiffness of the tumour, the inner block was made of the super-soft Ecoflex silicone rubbers [71], Ecoflex 00-10, 00-30 and 00-50, whose stiffnesses are 55.16 kPa, 68.95 kPa and 82.74 kPa, respectively. In total, there were six samples of tumours to be tested, i.e., Tumour-1-00-10, Tumour-2-00-10, Tumour-1-00-30, Tumour-2-00-30, Tumour-1-00-50 and Tumour-2-00-50. For each test, the pushing slide was manually pushed forward for a short distance from previous position. Once a test was finished, the pushing slide was reverted to its original place at where the capsule and the tumour were just in contact. To obtain reliable data, the pushing slide was locked with bolts until data recording was completed as shown in Fig. 7(c), and each test was repeated three times.

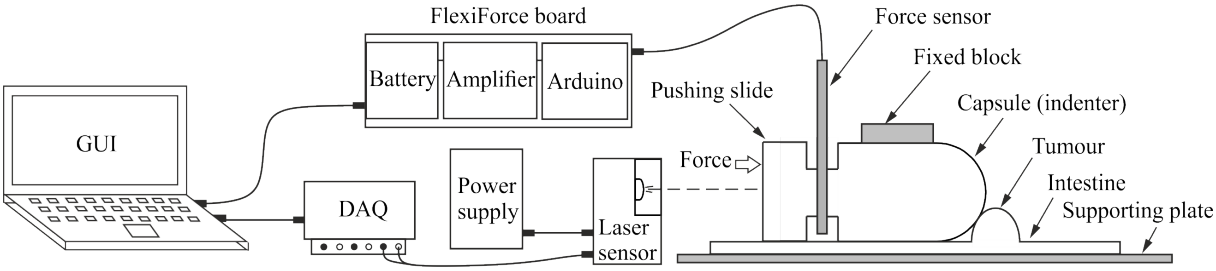

Figure 6: Schematic diagram of the experimental set-up for measuring the force-displacement curve of the capsule-tumour lateral contact. The pushing slide was used to push the capsule (indenter) forward in contact with the tumour. The lubricated indenter was restricted to horizontal movement. A force sensor was placed between the pushing slide and the indenter to record the horizontal contact force between the indenter and the tumour, and the force signal was collected by an integrated microcontroller board (FlexiForce). Displacement of the indenter was measured by a laser sensor and was collected by a National Instrument data acquisition (DAQ) card (USB6210). The force and displacement signals were gathered in a graphic user interface (GUI) in LabVIEW and the FlexiForce software.

To test the capsule-tumour vertical contact, Instron testing machine was employed as shown in Fig. 7(d), and its detailed views are presented in Figs. 7(e) and (f). Tumour samples lie on a supporting plate and was vertically compressed by a flat and a spherical indenters made of polythene with 11 mm in diameter. To prevent the tumour from slipping, a thin sandpaper was placed between the intestine and the supporting plate. The dimension and the composing of the tumour are the same as that used in lateral contact tests. During the experiment, force-displacement data was collected and prepared for comparison.

4. Results and discussions

This section compares experimental, numerical and FE results for capsule-tumour lateral and vertical contacts. Typical force-displacement curves for each contact case are presented to describe their consistencies, where the results of capsule-tumour lateral contact are shown in Fig. 8 and the results of vertical compression contact are presented in Figs. 9, 10 and 11. In addition, FE contour maps of tumour displacement shown in Fig. 12 are used to explain tumour deformation under different loading configurations.

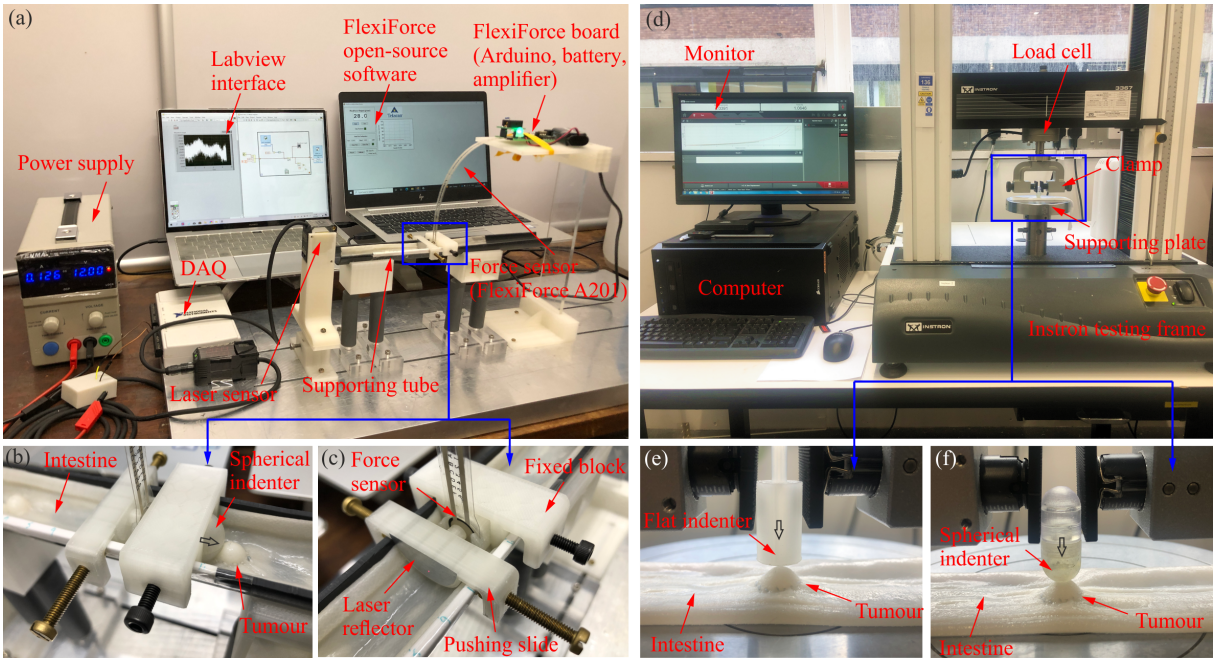

Figure 7: (a) Photograph of experimental set-up for capsule-tumour lateral contact, detailed views of (b) lateral contact and (c) indenter fixing mechanism. (d) Photograph of experimental set-up for capsule-tumour vertical contact, detailed views of vertical contact by using (e) a flat and (f) a spherical indenters.

Based on the experimental results of the force (F_n) and displacement (t_n) of capsule-tumour lateral contact under 10% compressive strain, the Young's modulus of the tumour will be obtained from Eq. (13) using the Hertz contact theory. Other parameters in Eq. (13), such as R_e and F_c, depend on the size of the tumour and the coordinates of the capsule-tumour contact point P_1, which has been elaborated in Section 2.2. After obtaining Young's moduli of tumours with different stiffnesses from Eq. (13), they were substituted into FE models of the capsule-tumour lateral contact to generate their force-displacement curves, which were further compared with experimental fitting results to verify the effectiveness of the proposed model. Fig. 8 presents a detailed comparison of the force-displacement curves obtained by experiments and FE simulations. As indenter was pushed manually, the data points of each experimental test were limited, and each sample was repeatedly tested three times. Moreover, due to the limited data set around the initial contact point, it was difficult to ensure that the position of the indenter was at the critical point of contact force every time. Therefore, a preload guaranteed to be within 0.2 N was controlled for each test, and FE simulations were also ensured to have the same preload settings as the experiment.

In mathematical modelling, in addition to being modelled as an ellipsoid, the tumour was also considered a sphere with a radius being the length of the semi-minor axis of the ellipsoid and a sphere with radius P_1P_2 shown in Fig. 3(c). Thus, FE results for the sphere-ellipsoid and the sphere-sphere lateral contact models were compared. For each stiffness, two tumour samples (Tumour-1 and Tumour-2) were fabricated and used for testing. Fig. 8 presents all the results of these samples made up of Ecoflex-00-10, 00-30 and 00-50. A power function ($y = g + hx^i$) indicated by red dashed line was used to perform nonlinear fitting on the experimental data as it fitted well with the experiment data compared with other functions. This can be attributed firstly to the fact that all the experimental data fall within the

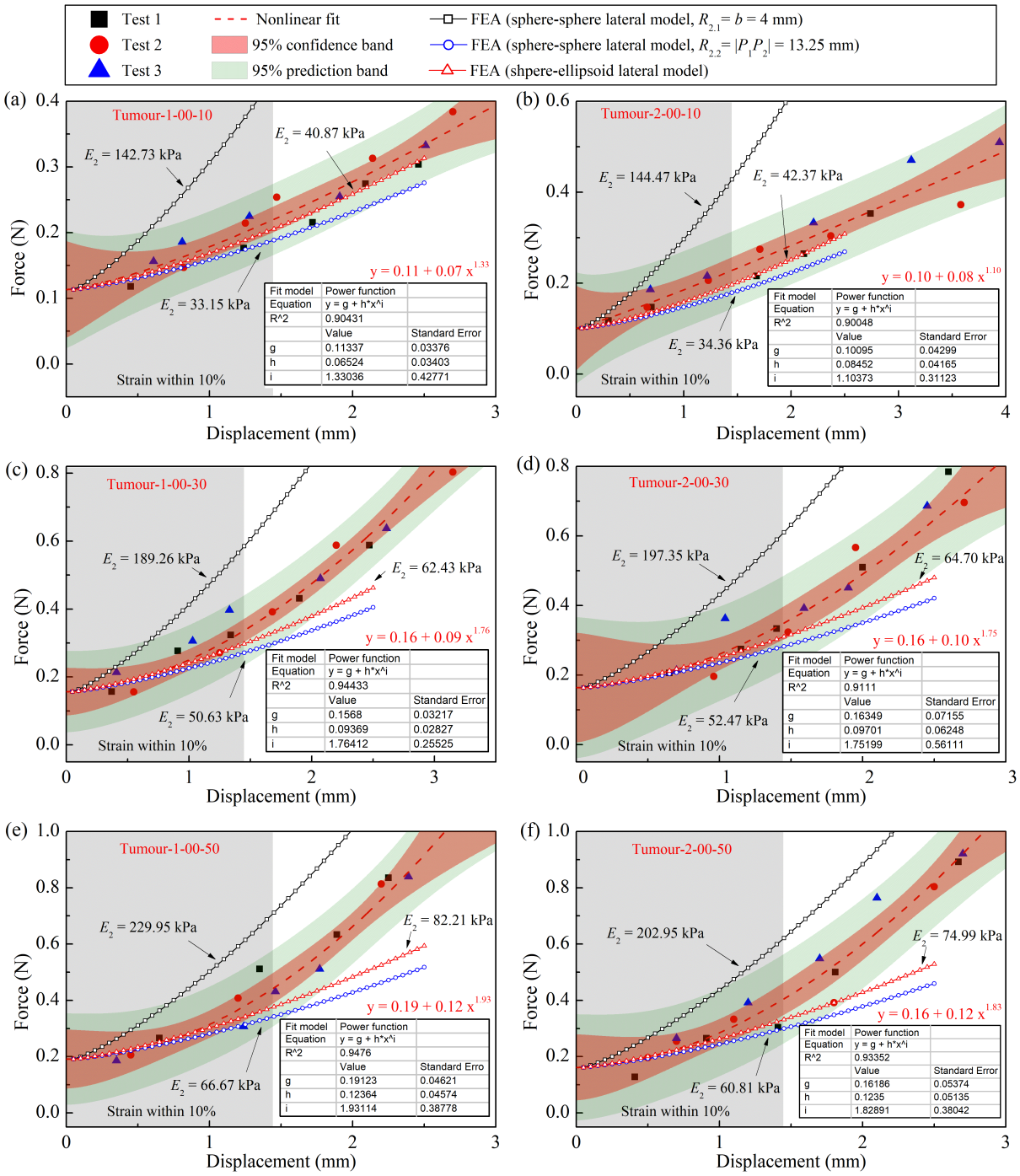

Figure 8: Comparison of force-displacement curves between FE simulations and experimental tests for capsule-tumour lateral contact with different samples of tumour: (a) Tumour-1-00-10, (b) Tumour-2-00-10, (c) Tumour-1-00-30, (d) Tumour-2-00-30, (e) Tumour-1-00-50 and (f) Tumour-2-00-50. Each sample was tested three times. Red dashed curves represent nonlinear fitting of the experiment data, and the red- and green-shaded areas are the 95% confidence band and the 95% prediction band of the fitting, respectively. Tables in subplots list the fitting parameters. Red triangles denote the FE results for sphere-ellipsoid lateral contact, and black squares and blue circles represent the FE results for sphere-sphere lateral contacts with $R_{2.1} = b = 4$ mm and $R_{2.2} = |P_1P_2| = 13.25$ mm, respectively. Grey-shaded areas indicate 10% of compressive strain in normal direction.

95% confidence and 95% prediction bands of the fitted curve represented by the red- and green-shaded areas, respectively. Furthermore, it can be observed from the tables in each subplot of Fig. 8 that the goodness-of-fit metrics, namely the coefficient of determination (denoted as R^2), were all greater than 0.9, indicating a high level of fitting accuracy and providing reliable results for the experimental data.

The comparison between the experimental fitting and FE results reveals that FE results of the sphere-ellipsoid lateral contact are in good agreement with the experimental results in small deformation range, despite some nuances between them. One of the main reasons for such a difference is considered to be the negligence of influence of the intestinal wall in the contact model, especially when the stiffness of the tumour bump is greater than the stiffness of the underlying intestinal wall. This can lead to an underestimation of tumour's stiffness. It can be seen from Fig. 8 that when the tumour is stiffer, the difference between the FE and the experimental results is greater. However, the present work only studied early bowel cancer (relatively less stiff) under a very small compression strain. Such a negligence might not be that significant. In addition, the strong nonlinearity observed in the experimental fitting results is due to (1) the uneven distribution of experimental points resulting in different intervals of different sample results being fitted, (2) tumour's inaccurate dimension control during fabrication causing different curvature radii at the capsule-tumour contact point, and (3) variations in the internal density of silicone rubber within tumour materials during fabrication process. In this study, within a small deformation range of 10%, tumour tissue was assumed to be an isotropic linear elastic solid, and the Hertz model was used to calculate tissue's stiffness.

By comparing with the FE results of the sphere-sphere lateral models with $R_{2.1} = 4$ mm and $R_{2.2} = 13.25$ mm, the force-displacement curves in Fig. 8 using the proposed sphere-ellipsoid lateral contact model are in good agreement with the experimental fitting curves within 10% compression strain. The sphere-sphere lateral model with $R_{2.1} = 4$ mm can be discarded as the force-displacement curve corresponding to its Young's modulus deviates from the experimental results completely. On the contrary, FE results of the sphere-sphere lateral model with $R_{2.2} = 13.25$ mm are very close to the experimental results, but its Young's modulus is still about 20% different from that of the sphere-ellipsoid model. Therefore, Young's moduli of Tumour-1-00-10 and Tumour-2-00-10 were identified as 40.87 kPa and 42.37 kPa, Young's moduli of Tumour-1-00-30 and Tumour-2-00-30 are 62.43 kPa and 64.70 kPa, and Young's moduli of Tumour-1-00-50 and Tumour-2-00-50 are 82.21 kPa and 74.99 kPa, respectively. Another observation is that Young's modulus identified via lateral compression is very close to that of silicone rubbers (with Ecoflex 00-10 of 55.16 kPa, 00-30 of 68.95 kPa and 00-50 of 82.74 kPa) inside the synthetic tumours. Thus, the capsule-tumour lateral compression method proposed in the present study can estimate the stiffness of the bowel tumour through Hertz contact theory effectively.

In order to verify the effectiveness of the lateral contact model, classical vertical compression test was explored and compared with the lateral contact model. All the vertical compression results conducted by using a flat and a spherical indenters on Instron machine are presented in Fig. 9. As can be observed from the figure, there are nonlinearities between the vertical contact force and the deformation of the tumour. To consider a reasonable deformation between the capsule-tumour contact, 10% compressive strain was used to calculate Young's modulus of the tumour. Fig. 10 and Fig. 11 present the comparison results of force-displacement curves within 10% compressive strain by using the flat and the spherical indenters, respectively. All tumour samples were tested using the same samples as in the capsule-tumour lateral contact tests to keep the studies consistent. Young's moduli of the tumours obtained by Hertz contact theory using Eqs. (15) and (16) were substituted into the FE models and then generated force-

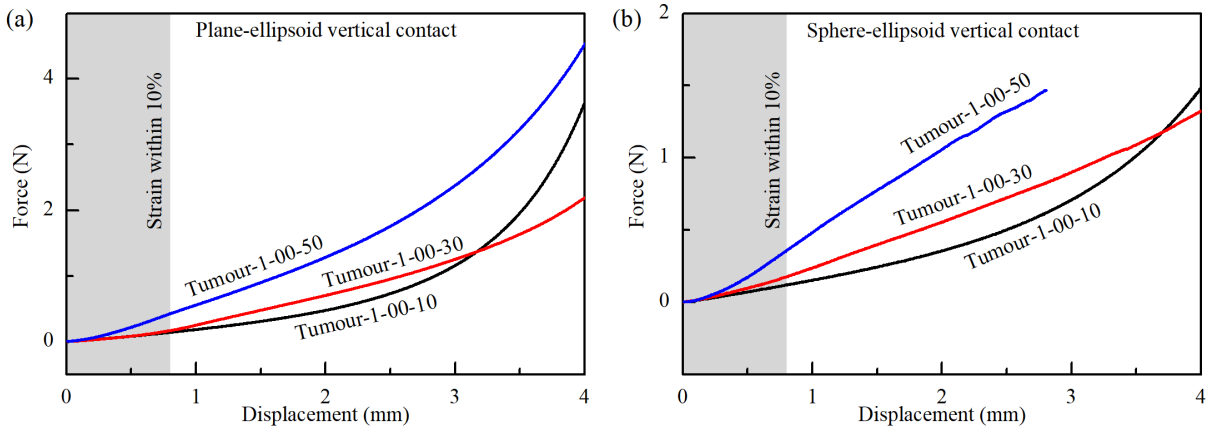

Figure 9: Force-displacement curves for (a) the plane-ellipsoid and (b) the sphere-ellipsoid vertical compression tests measured by an Instron machine. Grey-shaded areas represent the compressive strains within 10%.

displacement curves to compare with experimental results.

The comparative analyses are to start with the flat indenter compression shown in Fig. 10. By comparing the FE results for ellipsoidal tumours with those assuming spherical tumours, it is evident that the FE force-displacement curves obtained by using the Young's modulus of the ellipsoidal tumour are closer than the spherical one to the experimental result obtained by each test. As can be observed from the figure, Young's moduli of Tumour-1-00-10 and Tumour-2-00-10 are 80.09 kPa and 92.31 kPa, Young's moduli of Tumour-1-00-30 and Tumour-2-00-30 are 95.63 kPa and 104.53 kPa, and Young's moduli of Tumour-1-00-50 and Tumour-2-00-50 are 240.10 kPa and 262.29 kPa, respectively. It can be concluded that ellipsoidal model is more appropriate than the spherical one under vertical compression test. The reason for the slight discrepancy between the FE results of plane-ellipsoid normal contact and their experimental data is due to the challenge of achieving a perfect face-to-face fit between the bottom of the semi-ellipsoid tumour and the intestine during the suturing process of artificial tumours. This imperfect contact results in greater displacement under the same applied force during the vertical compression experiments. However, in the FE model, the manufacturing errors introduced during tumour fabrication were not taken into account. In addition, the difference in comparison results can be attributed to intestinal wall effects not being considered in the FE model under normal compression.

Fig. 11 presents the comparison results of force-displacement curves by using the spherical indenter. As can be seen from the figure, Young's modulus results of the sphere-ellipsoid vertical contact are more accurate than the sphere-sphere ones for which Tumour-1-00-10 and Tumour-2-00-10 are 79.38 kPa and 80.63 kPa, Tumour-1-00-30 and Tumour-2-00-30 are 115.36 kPa and 95.30 kPa, and Tumour-1-00-50 and Tumour-2-00-50 are 235.84 kPa and 256.70 kPa, respectively, and these measurements are consistent with the plane-ellipsoid vertical contact results.

In summary, the proposed sphere-ellipsoid lateral contact model can effectively measure the stiffness of the tumour when the capsule is in contact with the tumour. Ellipsoidal tumours cannot be assumed to be spherical under either lateral or vertical compression. To compare the Young's moduli obtained from the lateral and vertical compression tests, tumour deformations in FE simulations under different loading configurations are presented in Fig. 12. As can be seen from Figs. 12(a) and (b), the tumour deforms along X-axis significantly with some minor deformations along Y-axis. However, tumour deformations under

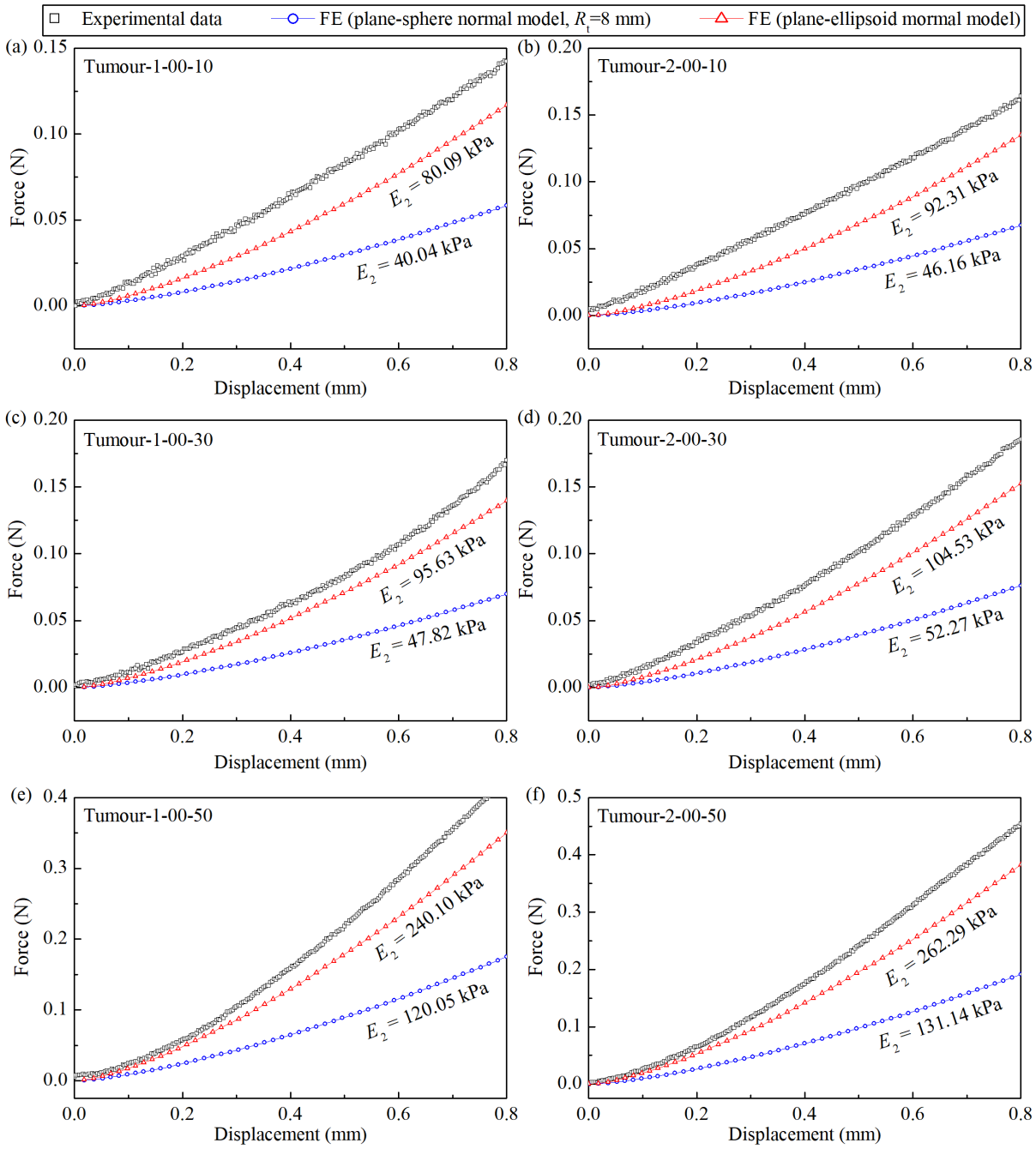

Figure 10: Comparison of force-displacement curves between FE results and experimental tests by using the flat indenter on (a) Tumour-1-00-10, (b) Tumour-2-00-10, (c) Tumour-1-00-30, (d) Tumour-2-00-30, (e) Tumour-1-00-50 and (f) Tumour-2-00-50. Black squares, red triangles and blue circles denote experimental results, FE results of plane-ellipsoid vertical contact and FE results of plane-sphere vertical contact with $R_t = 8$ mm, respectively.

vertical compression shown in Figs. 12(c) and (d) are only along Y-axis. Although both methods used 10% compression strain for calculation, the maximum deformation of the tumour under lateral contact in X-axis direction is larger than that under vertical contact in Y-axis direction. Thus, different deformations caused by their boundary conditions and compression directions may lead to different Young's moduli.

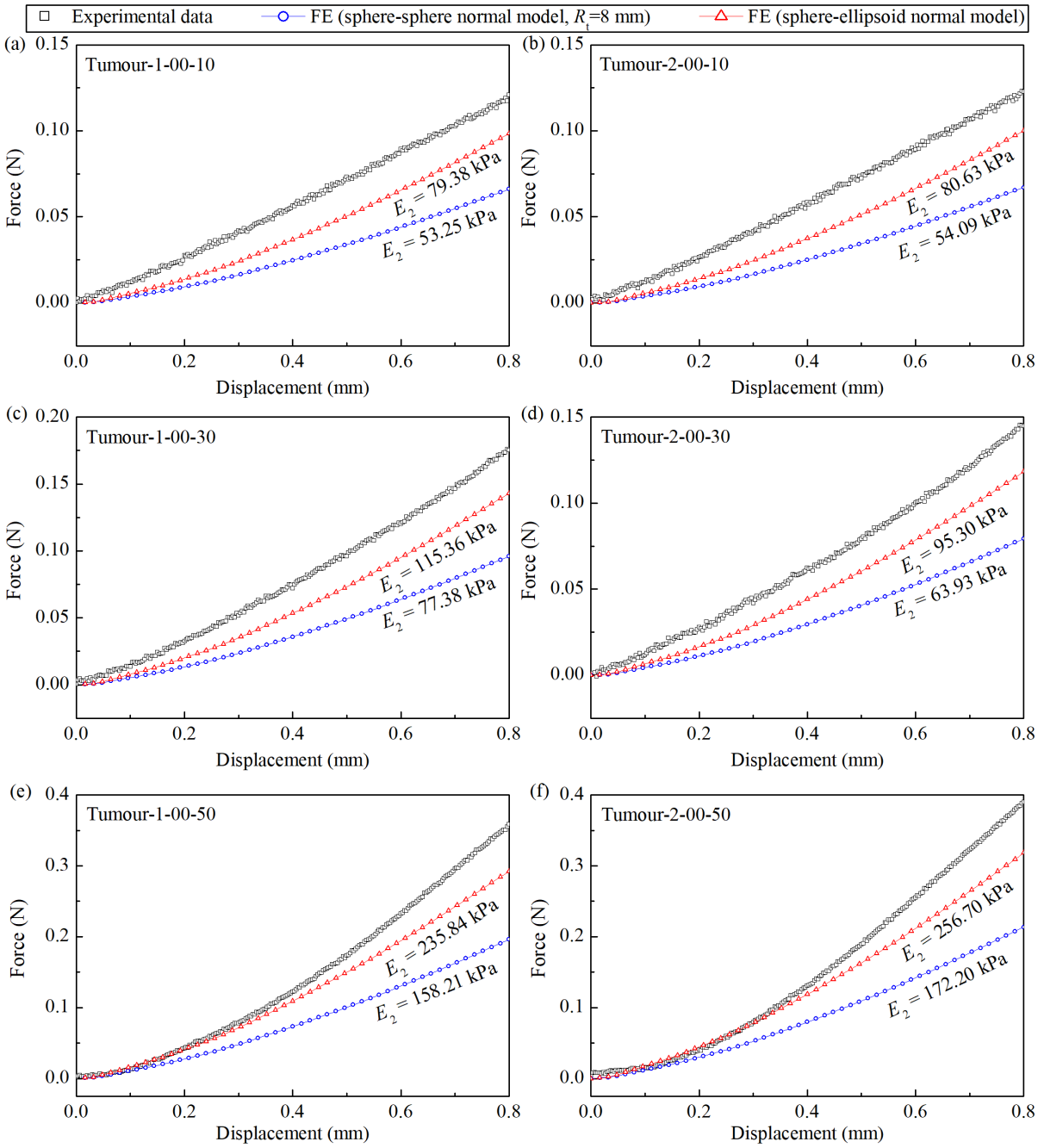

Figure 11: Comparison of force-displacement curves between FE results and experimental tests by using the spherical indenter on (a) Tumour-1-00-10, (b) Tumour-2-00-10, (c) Tumour-1-00-30, (d) Tumour-2-00-30, (e) Tumour-1-00-50 and (f) Tumour-2-00-50. Black squares, red triangles and blue circles represent experimental results, FE results of sphere-ellipsoid vertical contact and FE results of sphere-sphere vertical contact with $R_t = 8$ mm, respectively.

5. Conclusions and further works

Measuring the stiffness of bowel tumour by using a capsule robot for early bowel cancer detection was studied in this paper via mathematical and FE modelling in comparison with experimental investigation. Since both ends of the capsule robot are hemispherical and the morphology of the most common bowel

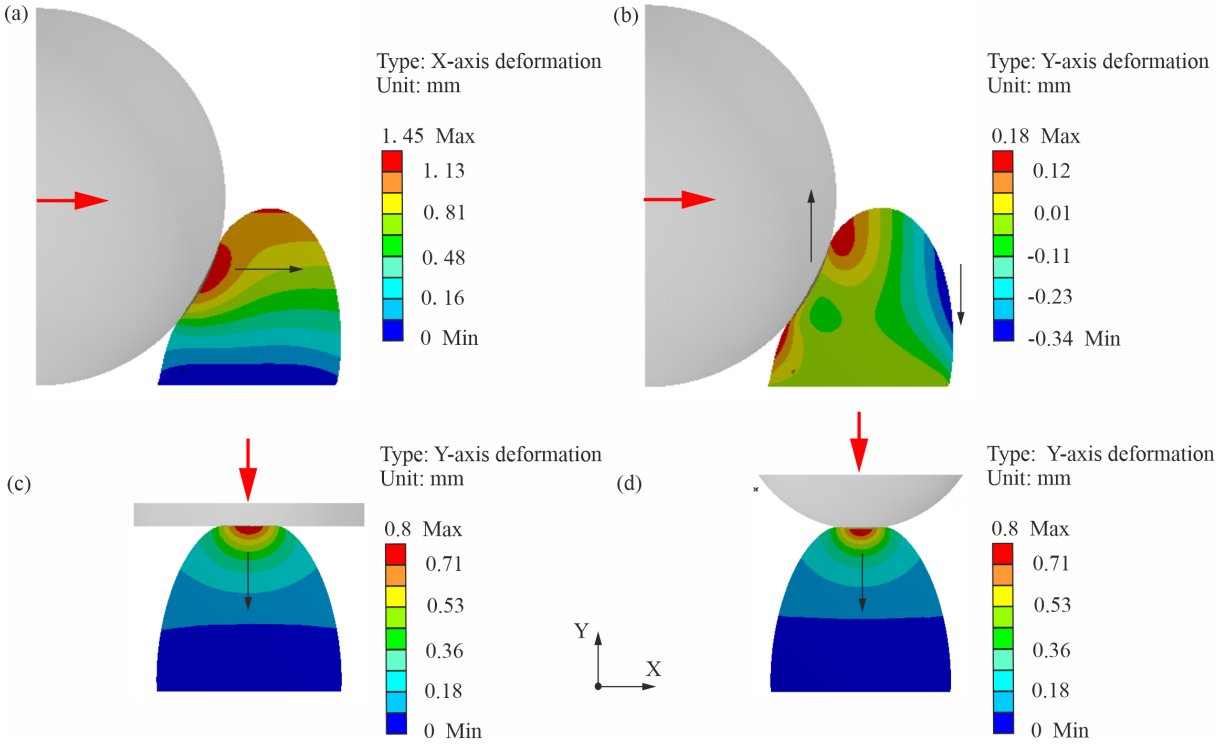

Figure 12: Deformations of the tumour under lateral compression along (a) X-axis and (b) Y-axis and vertical compression along Y-axis by using (c) the flat and (d) the spherical indenters.

tumour is quasi-semi-ellipsoidal, capsule-tumour lateral contact was modelled as sphere-ellipsoid contact by using Hertz contact theory. It was found that the proposed contact model can be used in real time to estimate the Young's modulus of the tumour when the capsule robot self-propels in the bowel.

After the preliminaries for characteristics of quadratic surfaces of both capsule head and tumour, Young's moduli of tumours were calculated based on Hertz contact theory and used in FE models to compare with experimental results. The comparison reveals that FE results of the sphere-ellipsoid lateral contact are in good agreement with experimental fitting results in the small deformation range, even though there are some differences due to the following reasons. Firstly, the FE and analytical models neglect the influence of the intestine wall, but in experiments, the deformation of the intestine wall can have slight effects on the results. The effect of the intestinal wall and its layers with different properties on the model will be studied as a future work. Secondly, with different stiffnesses of artificial tumour samples made of silicone materials, the experimental fitting results display a strong nonlinearity. This is mainly attributed to (1) the difference in fitting intervals of different sample results caused by the uneven distribution of experimental points, (2) the difference in curvature radius of the tumour at the contact point caused by the inaccurate dimension control in the process of tumour fabrication, and (3) different internal silicone rubber densities in tumour materials during its fabrication. Although these experimental uncertainties may cause inaccuracies in determining tumour's Young's modulus, the trends between the experiments and FE results are almost consistent under small deformations. This allows the lateral contact between the capsule and the tumour to effectively distinguish between different tumour stiffness levels. In normal compression, the difference between the FE and experimental results is due to

the same reason as the lateral contact mentioned above, and it is more obvious due to the uncertainty of tumour suturing. In addition, the results are always higher than the results of lateral contact as the latter causes distinct deformations in other directions. Based on the verification, ellipsoidal tumours cannot be assumed as spherical shapes due to the obvious difference between the FE and experimental results. After all, the proposed capsule-tumour lateral contact model can be used as a means to estimate the stiffness of bowel tumours.

Normal compression test is commonly used to measure the Young's modulus of cancerous tissue via *ex vivo*. However, it is difficult to apply *in vivo* in real time. The lateral contact method by using a capsule robot proposed in this paper can effectively solve this problem. Once the dimension of the tumour is pre-screened using a video camera via capsule endoscopy, the stiffness of the cancerous tissue can be estimated when the capsule is in contact with the tumour. This provides an advantageous means for clinicians to obtain this biological information during capsule endoscopy. For future work, experimental implementation of calculating tumour's stiffness in real time during capsule-tumour interaction will be carried out. The measurement will be achieved by attaching a force sensor to capsule head and using an external displacement sensor through magnetic "sensing" [72].

Acknowledgements

This work was supported by the EPSRC under Grant No. EP/V047868/1 and the Royal Society under Grant No. IEC/NSFC/201059. Mr Jiyuan Tian would like to acknowledge the financial support from China Scholarship Council for his CSC-Exeter PhD scholarship (award no. 201908060172). Mr Haohao Bi would like to acknowledge the financial support from the China Scholarship Council (award no. 202006290118) for his one-year visiting study at the University of Exeter. Professor Caishan Liu would like to acknowledge the financial support from the National Natural Science Foundation of China under Grant No. 11932001.

Compliance with ethical standards.

Conflict of interest. The authors declare that they have no conflict of interest concerning the publication of this manuscript.

Data availability. The datasets generated and analysed during the current study are not publicly available due to their massive size for editing and uploading, but will be available from the corresponding author on reasonable request.

References

[1] Y.-H. Xie, Y.-X. Chen, J.-Y. Fang, Comprehensive review of targeted therapy for colorectal cancer, Signal Transduction and Targeted Therapy 5 (1) (2020) 22.

[2] P. Kanth, J. M. Inadomi, Screening and prevention of colorectal cancer, The British Medical Journal 374 (2021).

[3] E. Dekker, P. J. Tanis, J. L. A. Vleugels, P. M. Kasi, M. B. Wallace, Colorectal cancer, The Lancet 394 (10207) (2019) 1467–1480. doi:https://doi.org/10.1016/S0140-6736(19)32319-0.
URL https://www.sciencedirect.com/science/article/pii/S0140673619323190

[4] C. R. UK, Bowel cancer incidence statistics, https://www.cancerresearchuk.org/health-professional/cancer-statistics/statistics-by-cancer-type/bowel-cancer, [Online; accessed: 13-02-2023] (2023).

[5] A. White, L. Ironmonger, R. J. Steele, N. Ormiston-Smith, C. Crawford, A. Seims, A review of sex-related differences in colorectal cancer incidence, screening uptake, routes to diagnosis, cancer stage and survival in the UK, BMC Cancer 18 (1) (2018) 1–11.

[6] A. Gini, E. E. Jansen, N. Zielonke, R. G. Meester, C. Senore, A. Anttila, N. Segnan, D. N. Mlakar, H. J. de Koning, I. Lansdorp-Vogelaar, et al., Impact of colorectal cancer screening on cancer-specific mortality in europe: a systematic review, European Journal of Cancer 127 (2020) 224–235.

[7] R. Cardoso, F. Guo, T. Heisser, M. Hackl, P. Ihle, H. De Schutter, N. Van Damme, Z. Valerianova, T. Atanasov, O. Majek, et al., Colorectal cancer incidence, mortality, and stage distribution in european countries in the colorectal cancer screening era: an international population-based study, The Lancet Oncology 22 (7) (2021) 1002–1013.

[8] M. Castelo, C. Sue-Chue-Lam, L. Paszat, T. Kishibe, A. S. Scheer, B. E. Hansen, N. N. Baxter, Time to diagnosis and treatment in younger adults with colorectal cancer: A systematic review, Plos One 17 (9) (2022) e0273396.

[9] A. Malki, R. A. ElRuz, I. Gupta, A. Allouch, S. Vranic, A.-E. Al Moustafa, Molecular mechanisms of colon cancer progression and metastasis: recent insights and advancements, International Journal of Molecular Sciences 22 (1) (2020) 130.

[10] V. Aran, A. P. Victorino, L. C. Thuler, C. G. Ferreira, Colorectal cancer: epidemiology, disease mechanisms and interventions to reduce onset and mortality, Clinical Colorectal Cancer 15 (3) (2016) 195–203.

[11] J. Tian, K. O. Afebu, A. Bickerdike, Y. Liu, S. Prasad, B. J. Nelson, Fundamentals of bowel cancer for biomedical engineers, Annals of Biomedical Engineering (2023). doi:https://doi.org/10.1007/s10439-023-03155-8.

[12] A. Qaseem, C. J. Crandall, R. A. Mustafa, L. A. Hicks, T. J. Wilt, Screening for colorectal cancer in asymptomatic average-risk adults: a guidance statement from the american college of physicians, Annals of Internal Medicine 171 (9) (2019) 643–654.

[13] W. M. Grady, S. D. Markowitz, The molecular pathogenesis of colorectal cancer and its potential application to colorectal cancer screening, Digestive Diseases and Sciences 60 (2015) 762–772.

[14] K. Bishay, N. Causada-Calo, M. A. Scaffidi, C. M. Walsh, J. T. Anderson, A. Rostom, C. Dube, R. N. Keswani, S. J. Heitman, R. J. Hilsden, et al., Associations between endoscopist feedback and improvements in colonoscopy quality indicators: a systematic review and meta-analysis, Gastrointestinal Endoscopy 92 (5) (2020) 1030–1040.

[15] Y. Liu, J. Tian, L. Manfredi, B. S. Terry, S. Prasad, I. Rahman, W. Marlicz, A. Koulaouzidis, A survey of small bowel modelling and its applications for capsule endoscopy, Mechatronics 83 (2022) 102748.

[16] A. Mittal, M. Kaur, et al., Computer-aided-diagnosis in colorectal cancer: A survey of state of the art techniques, in: 2016 International Conference on Inventive Computation Technologies (ICICT), Vol. 1, IEEE, 2016, pp. 1–6.

[17] Y. Luo, Y. Zhang, M. Liu, Y. Lai, P. Liu, Z. Wang, T. Xing, Y. Huang, Y. Li, A. Li, et al., Artificial intelligence-assisted colonoscopy for detection of colon polyps: a prospective, randomized cohort study, Journal of Gastrointestinal Surgery 25 (2021) 2011–2018.

[18] R. M. Summers, Polyp size measurement at ct colonography: what do we know and what do we need to know?, Radiology 255 (3) (2010) 707–720.

[19] J. Silva, A. Histace, O. Romain, X. Dray, B. Granado, Toward embedded detection of polyps in wce images for early diagnosis of colorectal cancer, International Journal of Computer Assisted Radiology and Surgery 9 (2014) 283–293.

[20] S. Hwang, J. Oh, W. Tavanapong, J. Wong, P. C. De Groen, Polyp detection in colonoscopy video using elliptical shape feature, in: 2007 IEEE International Conference on Image Processing, Vol. 2, IEEE, 2007, pp. II–465.

[21] Y. Fang, D. Zhu, J. Yao, Y. Yuan, K.-Y. Tong, Abc-net: Area-boundary constraint network with dynamical feature selection for colorectal polyp segmentation, IEEE Sensors Journal 21 (10) (2020) 11799–11809.

[22] H. A. Qadir, J. Solhusvik, J. Bergsland, L. Aabakken, I. Balasingham, A framework with a fully convolutional neural network for semi-automatic colon polyp annotation, IEEE Access 7 (2019) 169537–169547.

[23] Y. Zhang, G. Zhang, Z. Zeng, K. Pu, Activatable molecular probes for fluorescence-guided surgery, endoscopy and tissue biopsy, Chemical Society Reviews 51 (2) (2022) 566–593.

[24] O. O. Ogunwobi, F. Mahmood, A. Akingboye, Biomarkers in colorectal cancer: current research and future prospects, International Journal of Molecular Sciences 21 (15) (2020) 5311.

[25] T. Fuhs, F. Wetzel, A. W. Fritsch, X. Li, R. Stange, S. Pawlizak, T. R. Kießling, E. Morawetz, S. Grosser, F. Sauer, et al., Rigid tumours contain soft cancer cells, Nature Physics 18 (12) (2022) 1510–1519.

[26] J. Zhang, C. A. Reinhart-King, Targeting tissue stiffness in metastasis: mechanomedicine improves cancer therapy, Cancer Cell 37 (6) (2020) 754–755.

[27] Y. Shen, T. Schmidt, A. Diz-Muñoz, Protocol on tissue preparation and measurement of tumor stiffness in primary and metastatic colorectal cancer samples with an atomic force microscope, STAR Protocols 1 (3) (2020) 100167.

[28] P. Deptula, D. Lysik, K. Pogoda, M. Ciesluk, A. Namiot, J. Mystkowska, G. Krol, S. Gluszek, P. A. Janmey, R. Bucki, Tissue rheology as a possible complementary procedure to advance histological diagnosis of colon cancer, ACS Biomaterials Science & Engineering 6 (10) (2020) 5620–5631.

[29] M. Sugimoto, S. Takahashi, M. Kojima, N. Gotohda, Y. Kato, S. Kawano, A. Ochiai, M. Konishi, What is the nature of pancreatic consistency? assessment of the elastic modulus of the pancreas and comparison with tactile sensation, histology, and occurrence of postoperative pancreatic fistula after pancreaticoduodenectomy, Surgery 156 (5) (2014) 1204–1211.

[30] M. K. Loft, M. R. V. Pedersen, H. B. Rahr, S. R. Rafaelsen, Can ultrasound elastography discriminate between rectal adenoma and cancer? a systematic review, Cancers 13 (16) (2021) 4158.

[31] H. M. Kim, S. Yang, J. Kim, S. Park, J. H. Cho, J. Y. Park, T. S. Kim, E.-S. Yoon, S. Y. Song, S. Bang, Active locomotion of a paddling-based capsule endoscope in an in vitro and in vivo experiment (with videos), Gastrointestinal Endoscopy 72 (2) (2010) 381–387.

[32] Z.-J. Sun, B. Ye, Y. Qiu, X.-G. Cheng, H.-H. Zhang, S. Liu, Preliminary study of a legged capsule robot actuated wirelessly by magnetic torque, IEEE Transactions on Magnetics 50 (8) (2014) 1–6.

[33] J. Gao, G. Yan, Locomotion analysis of an inchworm-like capsule robot in the intestinal tract, IEEE Transactions on Biomedical Engineering 63 (2) (2015) 300–310.

[34] R. Carta, G. Tortora, J. Thoné, B. Lenaerts, P. Valdastri, A. Menciassi, P. Dario, R. Puers, Wireless powering for a self-propelled and steerable endoscopic capsule for stomach inspection, Biosensors and Bioelectronics 25 (4) (2009) 845–851.

[35] F. Zhang, Z. Li, Y. Duan, A. Abbas, R. Mundaca-Uribe, L. Yin, H. Luan, W. Gao, R. H. Fang, L. Zhang, et al., Gastrointestinal tract drug delivery using algae motors embedded in a degradable capsule, Science Robotics 7 (70) (2022) eabo4160.

[36] D. Ye, J. Xue, S. Yuan, F. Zhang, S. Song, J. Wang, M. Q.-H. Meng, Design and control of a magnetically-actuated capsule robot with biopsy function, IEEE Transactions on Biomedical Engineering 69 (9) (2022) 2905–2915.

[37] A. Garcia Garcia de Paredes, S. A. Gross, A. H. Hernandez-Lara, S. L. Hansel, D. M. Poppers, E. Rajan, Colorectal cancer and polyp detection using a new preparation-free, colon-scan capsule: A pilot study of safety and patient satisfaction, Digestive Diseases and Sciences (2022) 1–8.

[38] X. Jia, X. Xing, Y. Yuan, L. Xing, M. Q.-H. Meng, Wireless capsule endoscopy: A new tool for cancer screening in the colon with deep-learning-based polyp recognition, Proceedings of the IEEE 108 (1) (2019) 178–197.

[39] V. Blanes-Vidal, G. Baatrup, E. S. Nadimi, Addressing priority challenges in the detection and assessment of colorectal polyps from capsule endoscopy and colonoscopy in colorectal cancer screening using machine learning, Acta Oncologica 58 (sup1) (2019) S29–S36.

[40] A. R. Robertson, S. Segui, H. Wenzek, A. Koulaouzidis, Artificial intelligence for the detection of polyps or cancer with colon capsule endoscopy, Therapeutic Advances in Gastrointestinal Endoscopy 14 (2021) 26317745211020277.

[41] M. W. Alam, S. S. Vedaei, K. A. Wahid, A fluorescence-based wireless capsule endoscopy system for detecting colorectal cancer, Cancers 12 (4) (2020) 890.

[42] Y. Liu, J. Paez Chavez, J. Zhang, J. Tian, B. Guo, S. Prasad, The vibro-impact capsule system in millimetre scale: numerical optimisation and experimental verification, Meccanica 55 (2020) 1885–1902.

[43] Y. Xu, K. Li, Z. Zhao, M. Q.-H. Meng, Autonomous magnetic navigation framework for active wireless capsule endoscopy inspired by conventional colonoscopy procedures, IEEE Robotics and Automation Letters 7 (2) (2022) 1729–1736.

[44] M. C. Hoang, K. T. Nguyen, V. H. Le, J. Kim, E. Choi, B. Kang, J.-O. Park, C.-S. Kim, Independent electromagnetic field control for practical approach to actively locomotive wireless capsule endoscope, IEEE Transactions on Systems, Man, and Cybernetics: Systems 51 (5) (2019) 3040–3052.

[45] Z. Li, M. C. Hoang, C.-S. Kim, E. Choi, D. Bang, J.-O. Park, B. Kang, Modular capsules with assembly and separation mechanism: Proof of concept, in: Actuators, Vol. 10, MDPI, 2021, p. 159.

[46] K.-K. Liu, Deformation behaviour of soft particles: a review, Journal of Physics D: Applied Physics 39 (11) (2006) R189.

[47] P. Ding, I. Norton, Z. Zhang, A. Pacek, Mechanical properties of gelatin-rich micro-particles, Journal of Food Engineering 86 (3) (2008) 307–314.

[48] Q. Zheng, H. Zhu, A. Yu, Finite element analysis of the contact forces between a viscoelastic sphere and rigid plane, Powder Technology 226 (2012) 130–142.

[49] K. Kildashti, K. Dong, B. Samali, Q. Zheng, A. Yu, Evaluation of contact force models for discrete modelling of ellipsoidal particles, Chemical Engineering Science 177 (2018) 1–17.

[50] N. Xydas, I. Kao, Modeling of contact mechanics and friction limit surfaces for soft fingers in robotics, with experimental results, The International Journal of Robotics Research 18 (9) (1999) 941–950.

[51] N. Xydas, M. Bhagavat, I. Kao, Study of soft-finger contact mechanics using finite elements analysis and experiments, in: Proceedings 2000 ICRA. Millennium Conference. IEEE International Conference on Robotics and Automation. Symposia Proceedings (Cat. No. 00CH37065), Vol. 3, IEEE, 2000, pp. 2179–2184.

[52] T. Inoue, S. Hirai, Elastic model of deformable fingertip for soft-fingered manipulation, IEEE Transactions on Robotics 22 (6) (2006) 1273–1279.

[53] Y. Zheng, A. F. Mak, Extraction of effective young's modulus of skin and subcutaneous tissues from manual indentation data, in: Proceedings of the 19th Annual International Conference of the IEEE Engineering in Medicine and Biology Society.'Magnificent Milestones and Emerging Opportunities in Medical Engineering'(Cat. No. 97CH36136), Vol. 5, IEEE, 1997, pp. 2246–2249.

[54] R. Tasseff, B. Aguilar, S. Kahan, S. Kang, C. C. Bascom, R. J. Isfort, An integrated multiscale, multicellular skin model, BioRxiv (2019) 830711.

[55] H. Hertz, Ueber die berührung fester elastischer körper., Journal für die Reine und Angewandte Mathematik (Crelle's Journal) (92) (1882) 156–171.

[56] Y. Tatara, Extensive theory of force-approach relations of elastic spheres in compression and in impact, Journal of Engineering Materials and Technology-transactions of The Asme 111 (1989) 163–168.

[57] K. L. Johnson, K. Kendall, a. Roberts, Surface energy and the contact of elastic solids, Proceedings of the Royal Society of London. A. Mathematical and Physical Sciences 324 (1558) (1971) 301–313.

[58] G. Kuwabara, K. Kono, Restitution coefficient in a collision between two spheres, Japanese Journal of Applied Physics 26 (8R) (1987) 1230–1233.

[59] R. D. Mindlin, Compliance of elastic bodies in contact, Journal of Applied Mechanics—Transactions of the ASME 16 (3) (1949) 259–268.

[60] R. D. Mindlin, H. Deresiewicz, Elastic spheres in contact under varying oblique forces, Journal of Applied Mechanics—Transactions of the ASME 20 (3) (1953) 327–344.

[61] M. I. Munteanu, A. I. Nistor, On the geometry of the second fundamental form of translation surfaces in e3, Houston Journal of Mathematics 37 (4) (2011) 1087–1102.

[62] W. Harris, Curvature of ellipsoids and other surfaces, Ophthalmic and Physiological Optics 26 (5) (2006) 497–501.

[63] M. P. Do Carmo, Differential geometry of curves and surfaces: revised and updated second edition, Dover Publications, Mineola, New York, USA, 2016.

[64] Q. Zheng, Z. Zhou, A. Yu, Contact forces between viscoelastic ellipsoidal particles, Powder Technology 248 (2013) 25–33.

[65] L. Barducci, J. C. Norton, S. Sarker, S. Mohammed, R. Jones, P. Valdastri, B. S. Terry, Fundamentals of the gut for capsule engineers, Progress in Biomedical Engineering 2 (4) (2020) 042002.

[66] J. Rheinlaender, A. Dimitracopoulos, B. Wallmeyer, N. M. Kronenberg, K. J. Chalut, M. C. Gather, T. Betz, G. Charras, K. Franze, Cortical cell stiffness is independent of substrate mechanics, Nature materials 19 (9) (2020) 1019–1025.

[67] K. L. Johnson, Contact mechanics, Cambridge university press, Cambridge, UK, 1985. doi:https://doi.org/10.1017/CBO9781139171731.

[68] L. C. Hale, Principles and techniques for designing precision machines, Ph.D. thesis, Lawrence Livermore National Lab, University of California, Livermore, California, United States (1999).

[69] J. Zhang, Y. Liu, D. Zhu, S. Prasad, C. Liu, Simulation and experimental studies of a vibro-impact capsule system driven by an external magnetic field, Nonlinear Dynamics 109 (3) (2022) 1501–1516.

[70] Syndaver labs: Small intestine, accessed on 28th February 2023.
URL `http://syndaver.com/shop/syndaver`

[71] Smooth-On, Ecoflex series: Super soft silicone rubber, accessed on 28th February 2023.
URL https://www.benam.co.uk/products/silicone/addition/ecoflex

[72] Y. Xu, K. Li, Z. Zhao, M. Meng, Adaptive simultaneous magnetic actuation and localization for WCE in a tubular environment, IEEE Transactions on Robotics 38 (5) (2022) 2812–2826.